

Climatology and interannual variability simulated by the ARPEGE-OPA coupled model

L. Terray¹, O. Thual¹, S. Belamari¹, M. Déqué², P. Dandin^{3*}, P. Delecluse³, C. Lévy³

¹ Climate Modelling and Global Change Project, Cerfacs, 42, Avenue Gustave Coriolis, 31057 Toulouse Cedex, France

² Météo-France, Centre National de Recherches Météorologiques, 42, Avenue Gustave Coriolis, 31057 Toulouse Cedex, France

³ Laboratoire d'Océanographie Dynamique et de Climatologie – UMR 121, Université Pierre et Marie Curie – Case 100, 4, Place Jussieu, 75252 Paris Cedex 05, France

Received: 20 June 1994 / Accepted: 24 April 1995

Abstract. A 10-year simulation with a coupled ocean-atmosphere general circulation model (CGCM) is presented. The model consists of the climate version of the Météo-France global forecasting model, ARPEGE, coupled to the LODYC oceanic model, OPA, by the CERFACS coupling package OASIS. The oceanic component is dynamically active over the tropical Pacific, while climatological time-dependent sea surface temperatures (SSTs) are prescribed outside of the Pacific domain. The coupled model shows little drift and exhibits a very regular seasonal cycle. The climatological mean state and seasonal cycle are well simulated by the coupled model. In particular, the oceanic surface current pattern is accurately depicted and the location and intensity of the Equatorial Undercurrent (EUC) are in good agreement with available data. The seasonal cycle of equatorial SSTs captures quite realistically the annual harmonic. Some deficiencies remain including a weak zonal equatorial SST gradient, underestimated wind stress over the Pacific equatorial band and an additional inter-tropical convergence zone (ITCZ) south of the equator in northern winter and spring. Weak interannual variability is present in the equatorial SST signal with a maximum amplitude of 0.5° C.

state and the seasonal cycle are specified, produce interannual fluctuations and have been used as predictors for El Niño-Southern Oscillation (ENSO) events (Cane et al. 1986; Barnett et al. 1988).

Coupled GCMs (CGCMs) are potentially more realistic as they include a larger range of physical interactions and feedbacks within and between individual components. The apparent realism of uncoupled GCMs simulations dealing with ENSO phenomenon is very encouraging. For instance, the tropical atmospheric response to anomalous heating can be realistically reproduced in atmospheric GCMs (AGCMs) when the observed changes in boundary conditions are prescribed (Lau 1985; Palmer and Mansfield 1986; Mechoso et al. 1987; Stephenson and Royer 1994). The parallel success of oceanic GCMs (OGCMs) when forced by observed (Philander and Seigel 1985) or simulated winds (Dandin 1993; Belamari and Terray 1993) in reproducing oceanographic features of warm and cold events of the past decade is another source of optimism.

Nevertheless, as soon as one deals with coupled ocean-atmosphere simulations, the interface constraint is relaxed and most of these coupled GCMs show considerable drift and (or) unrealistic mean states as well as incorrect phases and amplitude for the seasonal cycle when it is included (Neelin et al. 1992). However, some coupled GCMs without seasonal cycle yield a mean state and interannual variations which bear some resemblance with observations (Philander et al. 1991). The next challenging step is to include the seasonal cycle in order to introduce the most important ocean-atmosphere interaction within the coupled system. This is necessary as there is observational and theoretical evidence which shows that the phase of the Southern Oscillation is strongly tied to that of the seasonal cycle. However, the relationship between annual and interannual variations is so far poorly understood and a great deal of work is being devoted to describe and understand the complexity of seasonal and interannual time scales in ocean-atmosphere CGCMs (Mechoso et al. 1995).

1 Introduction

The goal in developing general circulation models (GCMs) of the tropical Pacific ocean-global atmosphere is both to provide a forecasting tool and to investigate the physical mechanisms and instabilities at play within the coupled system. Simple models of the coupled ocean-atmosphere system in which the mean

* *Present address:* Météo-France, Centre National de Recherches Météorologiques, 42, Avenue Coriolis, 31057 Toulouse Cedex, France

Correspondence to: L. Terray

Despite these flaws, CGCMs are useful tools not only because they include the complete set of physical processes essential for the understanding of ocean-atmosphere energetics but also because they provide a consistent basis to analyze the physics and thermodynamics at work within each fluid. Thus, they suggest refinements for further development in model formulation and modelling assumptions.

The aim of this study is to provide a first description of the behaviour of a tropical Pacific ocean-global atmosphere coupled model from a 10-year simulation. The focus in this study is on the upper ocean and surface fluxes. A detailed analysis of atmospheric fields is underway and will be published in a forthcoming paper. Furthermore, the ARPEGE-OPA model is part of an intercomparison exercise of tropical GCMs whose results are published elsewhere (Mechoso et al. 1995). Section 2 briefly describes the coupled model. Section 3 presents the mean state and the seasonal cycle arising from the simulation and Section 4 deals with interannual variability. Finally, Section 5 concludes the paper with a summary and some directions for future work.

2 The ARPEGE/OPA coupled model

2.1 The ARPEGE model

The ARPEGE AGCM, from Météo-France, is a state-of-the-art spectral atmosphere model development from the ARPEGE/IFS forecast model and is described by Déqué et al. (1994). The model has 30 vertical levels extending up to 70 km (0.02 hPa) using a hybrid sigma-pressure vertical coordinate and has good resolution in the stratosphere. A triangular spectral T42 truncation has been used for horizontal resolution corresponding to a 2.8° grid size. The radiation scheme is both an extension and a simplification of the methods described in Geleyn and Hollingsworth (1979) with optical properties synthesized in a few coefficients following methods similar to those of Ritter and Geleyn (1992). The scheme is fast enough so that it can be called at each time step of the model. Both deep and shallow convection are parameterized. The deep convection uses a mass-flux scheme described by Bougeault (1985) while the shallow convection is parameterized with a modified Richardson number scheme described by Geleyn (1987). The exchange and drag coefficients for heat and momentum are computed according to Louis et al. (1982). Convective and stratiform cloudiness are calculated using the precipitation rates and the humidity profile. A two-layer prognostic soil temperature scheme is included in the model. The model time step is 15 minutes.

2.2 The OPA model

The OPA OGCM from the Laboratoire d'Océanographie DYnamique et de Climatologie (LODYC) (Delecluse et al. 1993) solves the primitive equations with a

non-linear equation of state (Millero and Poisson 1981; Unesco 1983). Those equations are discretized on a staggered C-grid using finite difference schemes. The use of vectorial operators relying on tensorial formalism ensures second-order accuracy on any curvilinear orthogonal grid (Marti et al. 1992). The discretization of the vorticity term in the momentum equation ensures the potential enstrophy conservation for any horizontal non-divergent flow. Time stepping for the advection, Coriolis and pressure terms is achieved by a basic leapfrog scheme associated with an Asselin filter applied at each time step in order to avoid time splitting. A forward scheme is used for horizontal diffusive processes and an implicit one for vertical diffusion. The model time step is one hour.

The code has been adapted to the tropical Pacific ocean (Dandin 1993). The model Pacific basin is bounded by closed western and eastern coastlines. Meridionally, the domain is closed at 40°S and 48°N, respectively. The horizontal resolution is 0.75° in longitude and between 0.33° and 1.5° in latitude (with the highest resolution near the equator). Twenty eight vertical levels are chosen with 17 levels in the upper 400 m. A gridded bathymetric data set of 5' × 5' (ETOP5 1986) resolution has been interpolated onto the model mesh. The abyssal trenches have been cut off at 4950 m and islands submerged at 700 m. Horizontal diffusion is harmonic and eddy coefficients for momentum and heat are equal to 10³ m² s⁻¹. A 1.5 order turbulent kinetic energy (TKE) closure scheme has been used to parameterize vertical mixing (Blanke and Delecluse 1993) and penetrative solar radiation is allowed to penetrate surface layers. Zero fluxes of heat and salt and no-slip conditions are applied at solid boundaries. The temperature and salinity fields are constrained to climatological values (Levitus 1982) with a restoring coefficient varying with depth as proposed by Sarmiento and Bryan (1982). The salinity restoring coefficient decreases exponentially from 4 days⁻¹ at the surface to 2 years⁻¹ at the ocean bottom. The temperature restoring coefficient increases from 0 at the sea surface to 13 days⁻¹ at 150 m and then decreases to 2 years⁻¹ at the bottom. This vertical profile is modified according to latitude and distance from the coast (Dandin 1993). It is multiplied by a function set to zero at the equator and increasing smoothly in latitude as done for the Atlantic ocean by Reverdin et al. (1991). This technique keeps the equatorial features free from an imposed climatology and Fujio and Imasato (1991) have shown that it prevents inconsistencies due to the geostrophic adjustment. Furthermore this avoids the sharp transition between the free and restored regions as in other models (e.g., Philander and Siegel 1985). The relaxation vanishes within a 1000 km of the coast. This allows the swift western boundary currents to adjust freely in regions where ageostrophic terms become important.

2.3 10-year simulation with the OASIS coupler

The ARPEGE and OPA models have been coupled with the OASIS coupler (Terry 1994) for a 10 year-period. The coupled model is forced by seasonally varying insolation. The coupler ensures the time synchronization between the two models and completes the spatial interpolations from one grid to another. The three programs run in parallel and exchange coupling fields once per day, averaging out the diurnal cycle. SST and sea ice extent (SIE) are given to the AGCM and surface fluxes of heat, momentum and fresh water to the OGCM. SST outside the Pacific domain and the SIE field are prescribed from an observed monthly climatology from the Center for Ocean-Land-Atmosphere – Climate Analysis Center (COLA-CAC) data set over the 1979–1988 period (Reynolds 1988). Modelled SSTs at the northern, southern and western boundary are modified to smooth out the transition between prescribed and simulated SST. The higher resolution SST is spatially averaged before being transferred to the AGCM. The surface fluxes are interpolated onto the OGCM grid using bicubic interpolation and without flux correction. However, the net heat flux is modified along the boundaries to be consistent with the SSTs in the blending regions. The integration begins on July 1st using atmospheric and oceanic initial fields simulated in the uncoupled model simulations (Déqué et al. 1994; Belamari and Terry 1993). These runs were performed as follows: the atmospheric one is an AMIP (Atmospheric Model Intercomparison Project)-type simulation where the ARPEGE model was forced with observed SSTs over the 1979–1988 period. The generated atmospheric fluxes were then used to drive the ocean model over the same period. The coupled run is carried out for 10 years and 6 months and the analysis relies upon the last 10 years of simulation. Many questions regarding the coupling strategy are still unanswered such as choosing the SST/flux exchange frequency, the influence of the initial state and the need for conservation constraints in interpolating schemes. These aspects are nevertheless beyond the scope of the present study and will be dealt with in a subsequent publication.

3 The mean state and the seasonal cycle

The mean state is defined as the total average over the 10-year analysis period. The mean seasonal cycle is defined in terms of averages for each calendar month over the same period. We first describe the mean state and the seasonal cycle for the surface fields before looking at the ocean interior. The Oberhuber (OBER) analysis of the COADS (Comprehensive Ocean-Atmosphere Data Set) data is used to provide a reference with which our results can be compared (Oberhuber 1988; Wright 1988).

3.1 The mean state

3.1.1 The ocean-atmosphere interface

Annual mean SST and error map relative to OBER are presented in Fig. 1a, b. The annual mean SST is too warm in the Eastern Pacific with a cold tongue about 2° C warmer than observations. It extends only to 160° W and is centered on the equator. North of the equator, the SST pattern shows warm waters along 10° N extending too far east. The main bias is characterized by a very warm SST in the eastern part just south of the equator during the “warm season” (from March through May) of the annual cycle. The warm pool SST is very homogeneous around 29° C which is close to values from OBER. However, warm temperatures (>28° C) penetrate eastward as far as 130° W in the south central Pacific. Finally, the upwelling off the coast of South America is not well simulated as is also the case in most OGCMs. The overall pattern is quite realistic despite too warm SSTs on the eastern side of the Pacific (up to 4° C along the coasts of Peru and California). It is interesting to compare the coupled results with the outputs from the uncoupled ocean simulation forced with AMIP fluxes. The warm tendency was already present in the uncoupled run (Belamari and Terry 1993) and is amplified by the coupling (not shown).

Figure 2 compares the annual mean for the two components of the modelled wind stress with the OBER data (Wright 1988). The simulated zonal stress is clearly too weak especially in the central Pacific (deviation up to .04 Pa). It is slightly larger along the Mexican coast. In the western Pacific, the modelled wester-

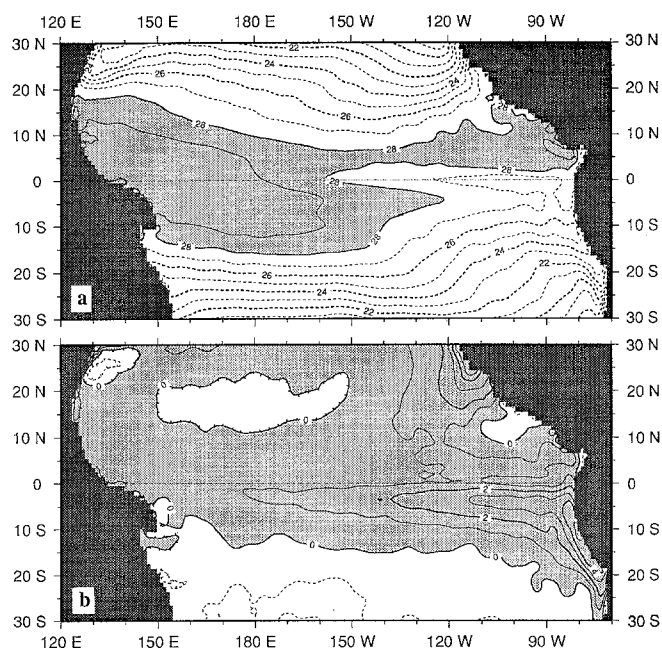


Fig. 1a. Simulated annual mean SST (°C). Contour interval is 1°C, shading above 28° C; **b** annual mean model SST error: CGCM minus OBER climatology; positive values are shaded

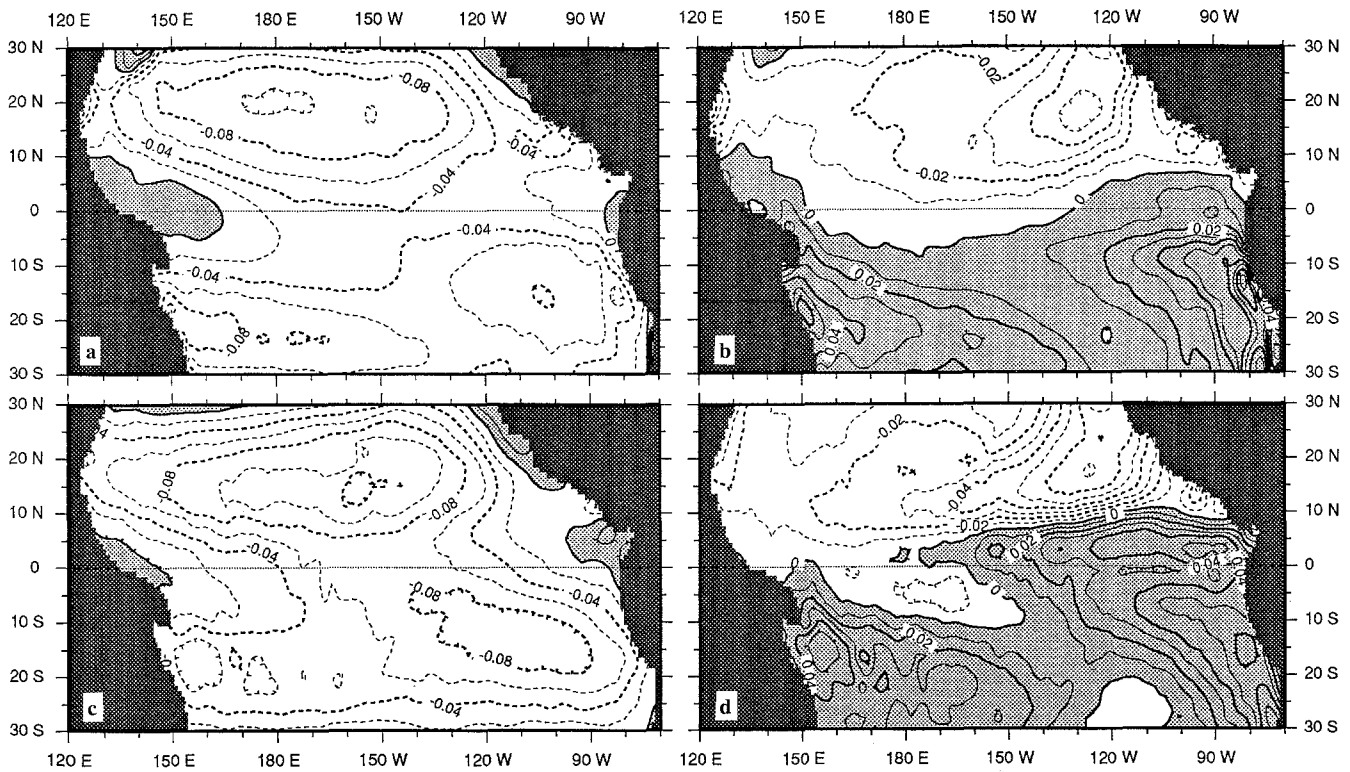


Fig. 2a–d. Zonal and meridional wind stress annual means (Pa). **a, b** simulated; **c, d** OBER climatology. Wind stress is southerly and westerly in shaded areas. Contour interval is 0.01 Pa

lies extend further east along the equator while they are weaker than the observed ones in the gulf of Panama. There are on-shore winds along the Chilean coast which could be related to the Gibbs phenomenon associated with the Andes in the atmospheric spectral model (Fig. 2a, c). The southerly component is also much smaller than the observed one in the central and eastern Pacific (Fig. 2b, d). Consequently, the cross-equatorial flow is strongly diminished. Similar results occurred when the AGCM was forced with observed SSTs in an AMIP-type experiment (Déqué et al. 1994). Figure 3 shows the annual mean of the wind curl and divergence from the simulation and the OBER data. The large-scale features of the curl field are well simulated by the model. The band of modelled positive curl north of the equator is slightly underestimated in the eastern and central Pacific (Fig. 3a, c). The simulated convergence zones are broader and weaker than the “observed” ones. In particular, the strength of the ITCZ in the east and central Pacific is severely underestimated. Conversely, the convergence is reinforced in the southeast Pacific. Furthermore, the narrow equatorial band of divergent winds has almost completely vanished in the simulated flow (Fig. 3b, d). The global underestimation of the wind stress magnitude in the equatorial belt could be due to problems in surface parameterization at low wind speeds leading to insufficient momentum and moisture exchange in this wind regime. For instance, local evaporation plays an important role in the warm pool region characterized by low wind speeds and weak advection. Accurate parameter-

ization of evaporation is then crucial in determining convective activity. Enhanced latent heat release over the warm pool can in turn generate a remote dynamical response of the atmosphere and give a more vigorous Walker circulation (Miller et al. 1991).

Figure 4 displays the net heat flux and solar radiation annual means as well as the error map. The net heat flux into the ocean is large in the eastern Pacific over the cold tongue area and along the South American coast. West of the dateline, the net surface flux is small due to attenuation of the short wave component by the cloud cover associated with strong precipitation and substantial latent heat flux (Fig. 4a, b). There is too much solar radiation over a large portion of the Pacific, especially in the subtropical anticyclonic regions where differences with OBER can be as large as 100 W m^{-2} (Fig. 4c, d). This deficiency is most likely caused by the lack of marine strato-cumulus cloud cover, particularly along the Peruvian and Californian coasts. The AGCM evaluates the stratiform cloud cover as a simple function of relative humidity, using a vertical critical humidity profile (Geleyn and Hollingsworth 1979). The lower tropical troposphere is known to be too dry in the ARPEGE model (Déqué et al. 1994) which could explain why it does not simulate any cloud in the eastern part of the subtropical highs. The drying of the lower levels is common in deep convective parameterization schemes using the mass flux concept as is the case with ARPEGE. It produces a positive feedback between the increase of evaporation and enhanced convective precipitation. This deficiency

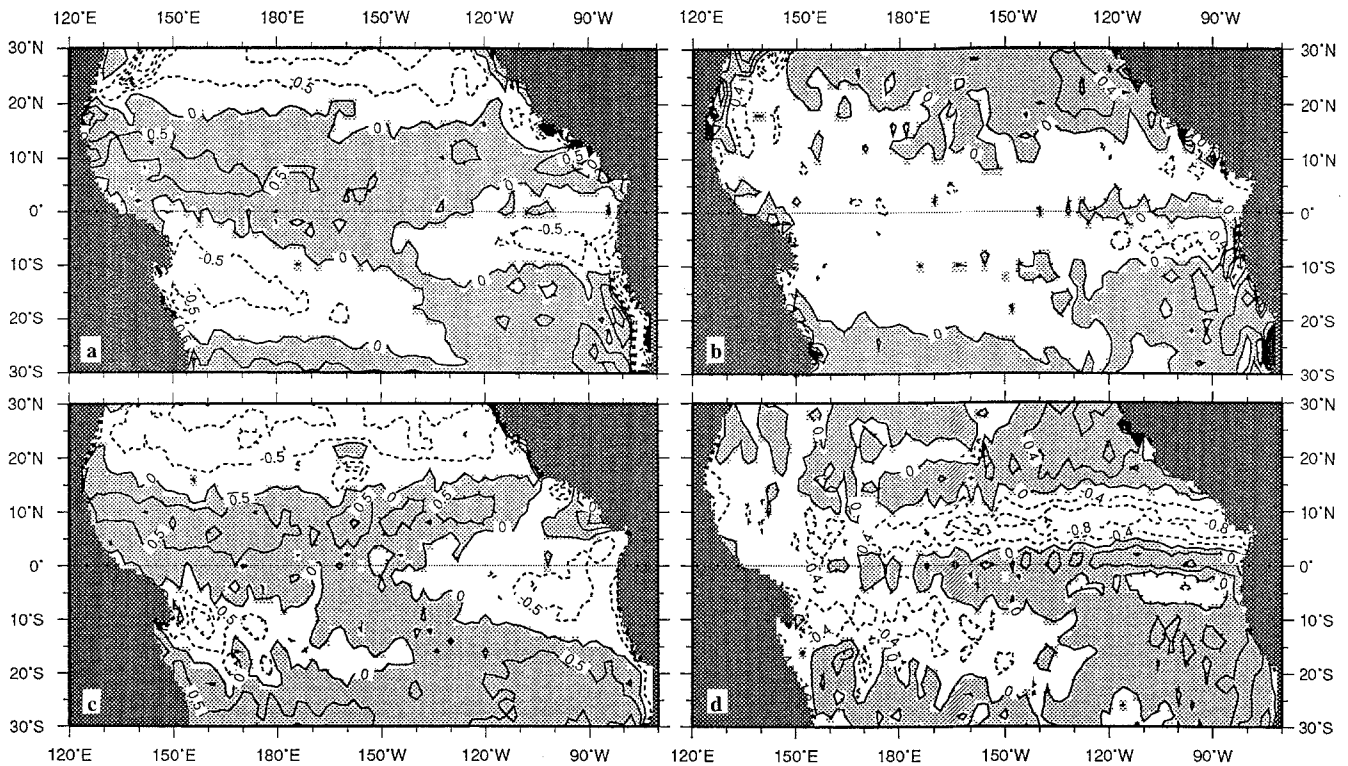


Fig. 3a–d. Annual mean wind stress curl and divergence (10^7 Pa m^{-1}). **a, b** Simulated; **c, d** OBER climatology. Positive values are shaded. Contour interval is $5 \times 10^6 \text{ Pa m}^{-1}$ for the curl and $4 \times 10^6 \text{ Pa m}^{-1}$ for divergence

could be corrected with a parameterization of the moistening associated to mesoscale convective downdrafts and evaporation of convective precipitation which are not accounted for in the model current version. This problem is partly responsible for the too high SST simulated in the underlying ocean regions by penetration of the short wave flux in the surface layers. The reasonable order of magnitude for the total heat flux hints at compensation through heat loss due to high temperatures generating strong latent and long wave heat fluxes.

The global precipitation and evaporation patterns are shown in Fig. 5a, b. The precipitation maxima delimitate the zones of deep convection and large-scale low level convergence associated with the highest SSTs. The ITCZ and the South Pacific Convergence Zone (SPCZ) are well depicted by the coupled model. Rainfall amount is large over the warm pool area implying increased convection compared to uncoupled AGCM results. A branch of tropical convergence appears south of the equator in the central and eastern Pacific. Although convection does occur south of the equator in the boreal spring, the mean simulated intensity is clearly overestimated (Waliser and Gautier 1993). This “double” ITCZ is a common feature of most coupled models (Mechoso et al. 1995) and a possible explanation will be presented in the next section. Evaporation is important in the trade wind maxima regions and has a broad minimum in the equatorial band across the entire Pacific basin.

3.1.2 Cross-sections through the ocean interior

The vertical structure of different oceanic quantities is presented in Figs. 6 and 7. The temperature pattern in the vertical section along the equator (Fig. 6a) shows the characteristic upward tilting of the isotherms in the eastern Pacific where the thermocline is shallow. In the western Pacific, the thermocline is deep and there is a well-homogenized mixed layer which is about 60 m deep. Figure 6b reveals the presence of a strong equatorial undercurrent EUC also tilting upward to the east. It is worth noting that its strength is correctly simulated. The core of the EUC is located between 110°W and 130°W at 80 m deep and its intensity is 1.2 m s^{-1} . At 140°W , the simulated EUC core is situated at 100 m and its intensity is 1.1 m s^{-1} which is in between the experimental values of Halpern and Weisberg (1989), 1.16 m s^{-1} , and those of McPhaden and McCarty (1992), 1.01 m s^{-1} . However it is overestimated at 110°W compared with observations, 1.18 m s^{-1} versus $.95 \text{ m s}^{-1}$, while its depth is in better agreement, 75 m versus 80 m. The weakness of the simulated zonal winds clearly suggests that the usual argument relying on the thermocline slope and the corresponding zonal pressure gradient (ZPG) as being the main driving force for the EUC fails to fully explain the simulated sub-surface flow intensity. A quantitative explanation would require a detailed study of the zonal momentum equation in order to determine the relative importance of the inertial, ZPG and friction terms at different locations.

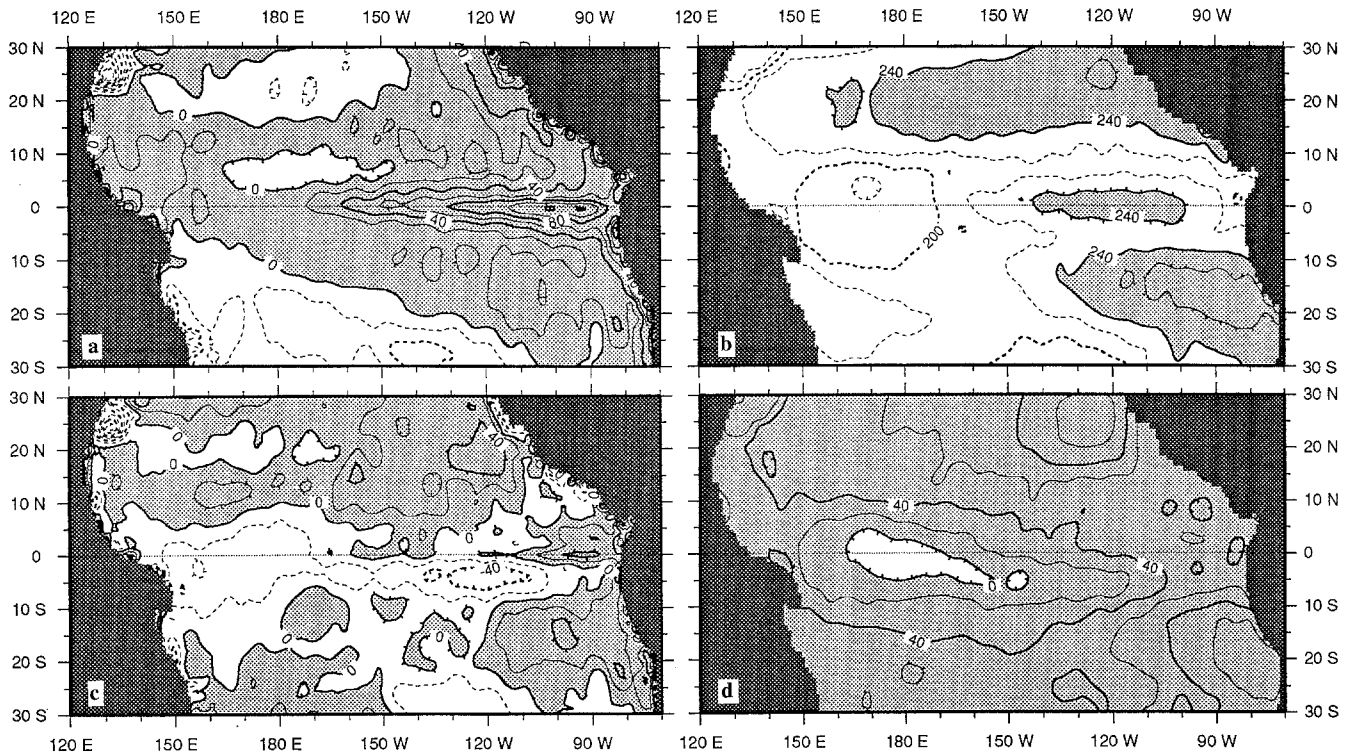


Fig. 4a–d. Simulated annual mean ($W m^{-2}$). **a** Total heat flux; positive values are shaded; **b** solar radiation; values above $240 W m^{-2}$ are shaded. Difference map: CGCM minus OBER climatology; **c** total heat flux; positive values are shaded; **d** solar radiation; positive values are shaded. Contour interval is $20 W m^{-2}$

logy; **c** total heat flux; positive values are shaded; **d** solar radiation; positive values are shaded. Contour interval is $20 W m^{-2}$

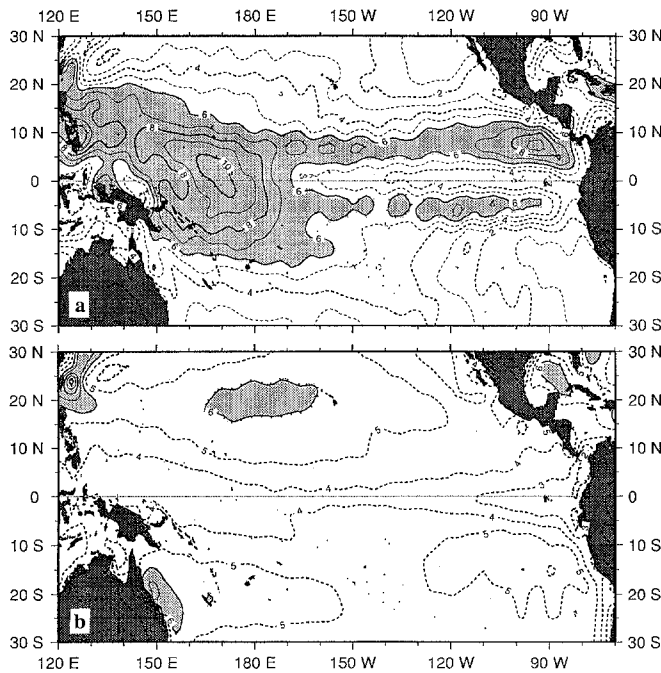


Fig. 5a, b. Simulated annual mean ($mm day^{-1}$) of **a** precipitation and **b** evaporation. Contour interval is $1 mm day^{-1}$ and values above $6 mm day^{-1}$ are shaded

The equatorial section of vertical velocity (Fig. 6c) depicts upwelling along the ocean basin except at around $150^{\circ}E$. The upwelling maximum is located between 50 and $75 m$ at $110^{\circ}W$ and its strength is about

$2 m day^{-1}$. The simulation gives an equatorial upwelling of $.83 m day^{-1}$ over the box $110^{\circ}W-140^{\circ}W/0-120 m$. Given the measurements uncertainty, this value is in rough agreement with observations of Halpern et al. (1989) who obtain $1.9 m day^{-1}$ for the same box. The eastern location of the simulated maxima is favored by the TKE parameterization which deepens the thermocline in the east and leads to an eastward penetration of the EUC (Blanke and Delecluse 1993) but also corresponds to the weak trades simulated regime.

The temperature structure in a meridional section near $150^{\circ}W$ (Fig. 7a) shows a ridge of the thermocline near $10^{\circ}N$ and a trough near $3^{\circ}N$ associated with the North Equatorial Countercurrent (NECC). These changes in the elevation of the thermocline are not as marked as in the observations from the Hawaii-Tahiti shuttle experiment (Wyrtki and Kilonski 1984). Rising of shallow equatorial isotherms suggests upwelling and westward flow. The zonal current structure is presented in Fig. 7b and consists of the westward South Equatorial Current (SEC) surrounded by two eastward currents, the NECC and its southern equivalent, the South Equatorial Countercurrent (SECC), and bounded below by the EUC. The westward current does not penetrate deeply ($70 m$) into the ocean north of the equator. This, linked with the weakly pronounced trough in the isotherms, indicates weak downwelling. Off the equator, Ekman theory gives the vertical velocity w_E as $w_E = (\nabla \times \tau) / f + \beta \tau_x / f^2$, where f is the Coriolis parameter and β its derivative with respect to y . $\nabla \times \tau$ and τ_x

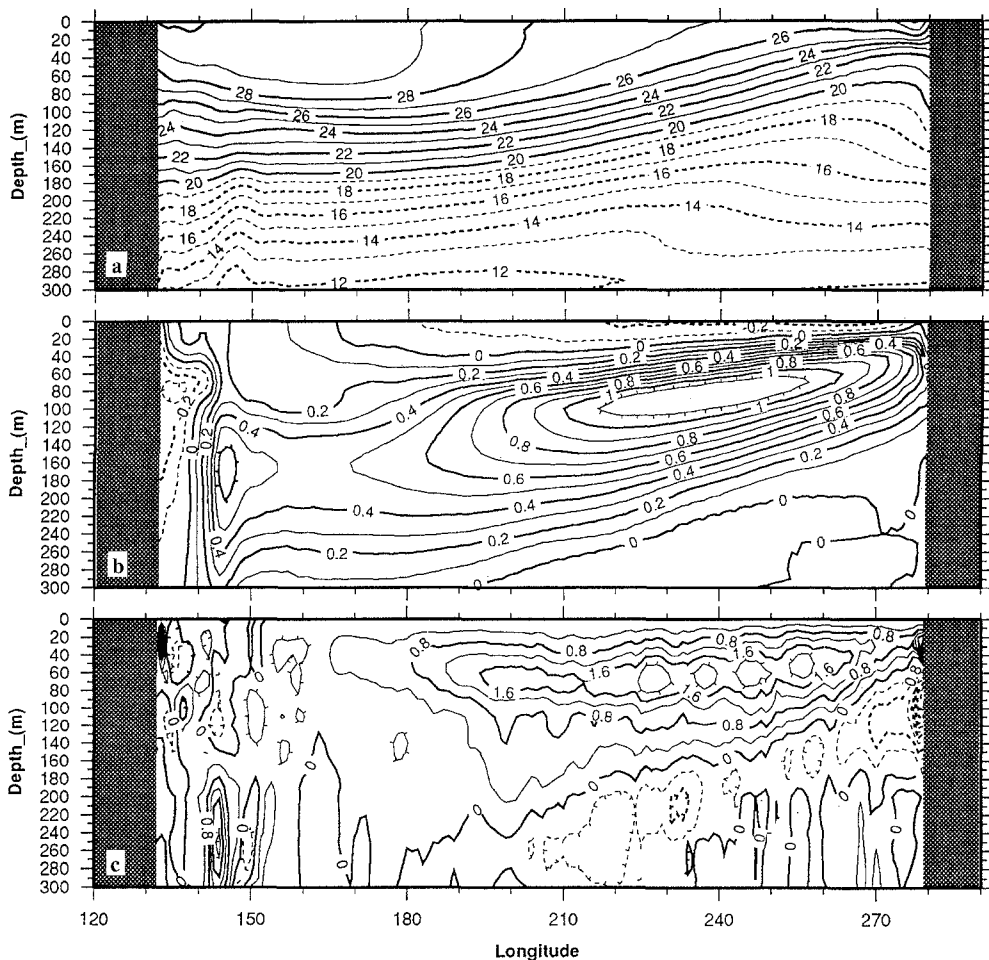


Fig. 6a-c. Equatorial depth-longitude sections of annual mean: **a** temperature ($^{\circ}\text{C}$) contour interval is 1°C ; **b** zonal current velocity (m s^{-1}) contour interval is 10 cm s^{-1} and *solid lines* indicate eastward current; **c** vertical current velocity (m day^{-1}) contour interval is 0.4 m day^{-1} and *solid (dashed)* contours indicate upwelling (downwelling)

are the wind stress curl and its zonal component. In the OBER data at 150°W , $\nabla \times \tau$ is negative from the equator up to 3°N and reaches high positive values between 5°N and 10°N (Fig. 3c). $\beta \tau_x / f^2$ is also negative north of the equator and its value decreases away from the equator. North of the equator, w_E has negative values and gives downwelling. North of 5°N , the balance is positive as $(\nabla \times \tau) / f \geq 0$ and $\beta \tau_x / f^2 = 0$ and upwelling occurs. In the coupled simulation, $\nabla \times \tau$ at 150°W is positive north of the equator (Fig. 3a) and the zonal wind stress is minimum on the equator or south of it before increasing steadily northward as shown by Fig. 2a. Just north of the equator, the terms $(\nabla \times \tau) / f$ and $\beta \tau_x / f^2$ have opposite signs with weak downwelling around 3°N resulting from larger negative values of the $\beta \tau_x / f^2$ term. $(\nabla \times \tau) / f$ becomes predominant north of 5°N up to 10°N and generates a weak upwelling. The weak meridional circulation near the equator shows the classical picture of Ekman divergence induced by easterly winds near the surface and geostrophic inflow at thermocline depths, indicating a linear response to the weak zonal winds (Fig. 7c).

3.2 The seasonal cycle

3.2.1 SST and zonal wind stress

Figure 8 displays the annual mean SST and the first harmonic of the annual variation in SST over the Pacific basin as in Horel (1982). The amplitude and phase of the annual cycle are displayed as arrows, with the arrow length and direction indicating the amplitude and the phase, respectively. The coupled model results (Fig. 8a) agree closely with the COLA-CAC data (Fig. 8b) as well as with the COADS climatology (Horel 1982). The amplitude of the annual cycle in SST increases away from the equator and is maximum in late summer or early fall in the extratropical latitudes of each hemisphere. In the west Pacific, the coupled model does simulate correctly the warm pool temperature and extension as well as its seasonal migration between both hemispheres. In the central and western equatorial Pacific, the observed annual variation of SST is weak compared to interannual variability changes and is correctly depicted by the model. However, the model annual cycle shows a 2-month phase lag in the central Pacific along the NECC path and a symmetric positive phase shift south of the equator. The coupled model overestimates the maximum amplitude of the annual cycle along the Californian coast and in the

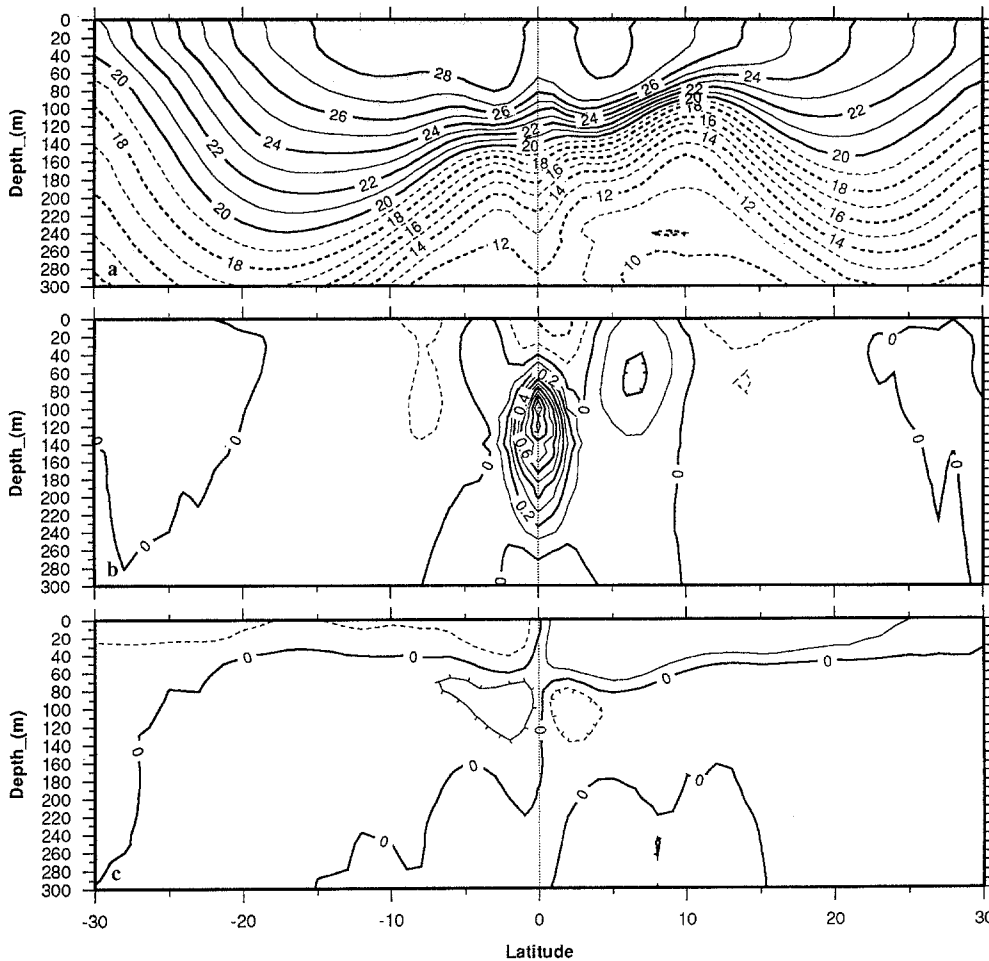


Fig. 7a–c. Meridional ocean cross-sections at 150°W of annual mean: **a** temperature (°C) contour interval is 1°C; **b, c** zonal and meridional current velocities (m s^{-1}) contour interval is 10 cm s^{-1} . *solid lines* indicate eastward and southward currents

Costa Rica warm pool. The main difference occurs along the front between the equatorial cold tongue and the Costa-Rica warm pool extending westward from the South American coast until 120°W. The modelled annual cycle lags behind the observed one along the northern fringe of the upwelling region by one and half months. Furthermore, the observed westward phase propagation of the SST in the eastern part of the equatorial wave guide is almost absent from the simulated annual cycle, especially south of the equator.

The seasonal cycle of simulated equatorial SST and zonal wind stress is compared to OBER in Fig. 9. There is good agreement between both SST fields especially in the eastern Pacific where the amplitude of the annual cycle is strong (Fig. 9a, b). The phase relationship between the seasonal migration of the warm pool and the seasonal cycle in the upwelling region is well depicted by the model. Furthermore, the model captures the weak semi-annual cycle in the west Pacific. However, it poorly simulates the transition between the warm phase (March–April) and the cold phase (August–October) as was previously mentioned. It shows little sign of westward propagation as well as an abrupt swing from one phase to another and a possible explanation for this biased transition is given in the next paragraph. The model fails to extend the cold phase late in the year. The westward propagation for the cold to warm phase transition is well represented.

Figure 9c, d shows westerly and easterly winds corresponding to warm and cold SSTs east of the dateline. Variability over the whole Pacific is clearly dominated in the simulation by the annual cycle of the northeast trades which penetrate south of the equator during northern winter. The signal amplitude is strongest in the western Pacific around 150°E with strong easterly and westerly anomalies in July–August and November–December, respectively. In the eastern Pacific the wind pattern shows westward propagation of westerly anomalies similar to the observed one in northern winter and spring. Standing easterly anomalies are simulated in northern summer in contrast with the slight observed westward propagation. The main difference between the observed and simulated variability lies in the eastern and central-east Pacific due to the anomalous southward displacement of the northeast trades. The model overestimates the first part of the semi-annual cycle in the central eastern Pacific (around 140°W) and underestimates the second one. The strong seasonal change in the winds between April and June in the eastern Pacific can promote a very rapid onset of the cold tongue through local equatorial upwelling and helps to explain the biased transition between the warm and cold phases.

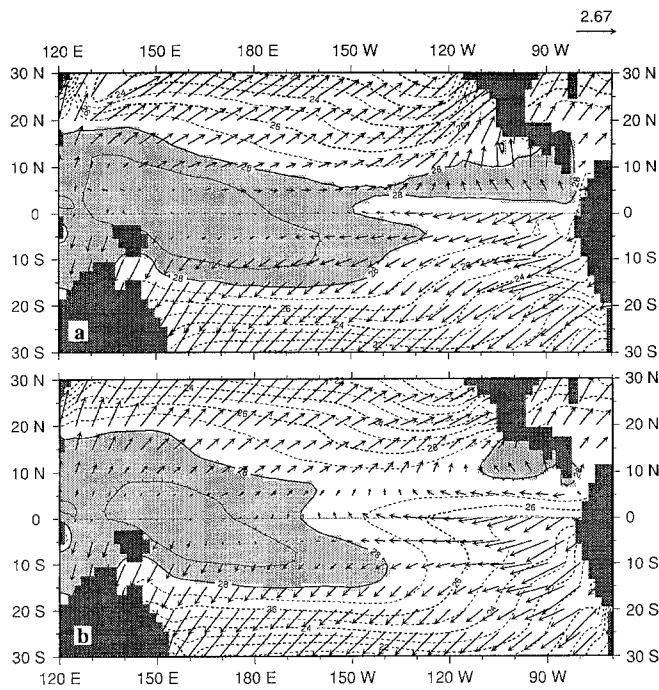


Fig. 8a, b. First harmonic of the annual variation in SST (arrows) superimposed upon the annual mean SST field (contours). The amplitude of the annual cycle is indicated by the *length* of the arrow according to the scale in the figure. The phase is indicated by the *direction* of the arrow. An arrow pointing from the top of the page indicates a maximum of SST on January 1st, from the right margin a maximum on April 1st, etc. Values above 28°C are shaded. The contour interval for the annual mean SST is 1°C. **a** coupled model and **b** COLA-CAC data set (1979–1993)

3.2.2 Upper ocean

Zonal cross-sections of simulated ocean temperature and zonal current along the equator appear in Fig. 10 for April and October. The thermocline deepens in April and shoals in October in the equatorial eastern Pacific. At 110°W, the 20°C isotherm is 80 and 50 m deep, respectively. The longitudinal position of the thermocline maximum east-west slope shifts eastward between April and October (Fig. 10a, b). In October the zonal slope of the thermocline in the far eastern Pacific reverses as the corresponding zonal surface winds are predominantly westerly. During the warm phase of the seasonal cycle, the EUC surges eastward at the equator as shown in Fig. 10c. In April, salty waters coming from the central Pacific advected by the SEC are subducted below the fresh surface waters, due to intense rainfall in the western Pacific during the southern summer. Surface currents attain their maxima in October in the eastern and central Pacific while the global EUC region deepens and its core shifts eastward related to the displacement of the thermocline maximum slope region. It induces an eastward extension of the EUC accelerative regime leading to high values around 115°W (Fig. 10d). In fact, the EUC intensity reaches its seasonal maximum in northern fall. Further analysis is needed to determine whether this is due to a local and/or global adjustment processes. For instance,

the equatorial zonal stress is at its minimum in October in the central east Pacific (around 150°W). This is a direct consequence of the exaggerated southward shift of the northeast trades in the northern winter and spring. This slackening of the zonal wind stress implies less vertical mixing in the upper layers. Since vertical turbulent diffusion acts as a brake on the EUC by transferring westward momentum from the surface, its weakening might be responsible for EUC maximum intensity further east. This could appear contradictory to the spring time surge of the EUC around 115°W which is related to a relaxation of the trades. Yet the zonal wind stress pattern exhibits a distinct though rather broad minimum at this exact location in space and time.

3.2.3 Eastern Pacific

As the coupled model main biases occur in the eastern Pacific, it is worth describing in detail the seasonal cycle of selected surface fields in this region. A time-latitude plot of the meridional wind stress averaged over the eastern Pacific [150°W–100°W] is presented in Fig. 11a. The northeast trades cross the equator from January to May and extend as far as 7°S. Indeed this behavior is related to the southward displacement of the ITCZ and to the presence of temperatures greater than 28°C over the southern part of the equatorial wave guide during the warm phase of the seasonal cycle (Fig. 11b). The precipitation field (Fig. 11c) has a strong rainfall maximum south of the equator in March–April linked to the low-level wind convergence previously mentioned. It also clearly indicates an overall increased rainfall amount in the same equatorial region compared to the uncoupled simulation (Fig. 11d). Exact simulation of the time-dependent behavior of the ITCZ-cold tongue structure is essential as it is the main seasonal feature in the eastern part of the tropical oceans (Mitchell and Wallace 1992). However, the majority of coupled GCMs are unable to maintain the ITCZ north of the equator through the year (Mechoso et al. 1995). Therefore, it is of considerable importance to explain why coupled GCMs perform so poorly in this aspect. It is interesting to notice that the uncoupled atmospheric simulation already shows a tendency towards a double ITCZ which is strongly amplified by the coupling. This highlights the primary role played by ocean-atmosphere feedbacks in the ITCZ shift. The following mechanism could be invoked to describe this phenomenon. Strong local heating and, to a lesser extent, ocean advection due to the presence of the SECC lead to warm SST south of the equator in the eastern Pacific during the warm phase of the seasonal cycle. Due to the onset of the Southern Hemisphere summer monsoon circulation, the belt of warm surface water could cause the land convection to spread westward to form an ITCZ. The weakness of the northward cross-equatorial flow could also play a role by failing to compete with the Southern Hemisphere continental monsoon belt. Further analysis is needed to test the validity

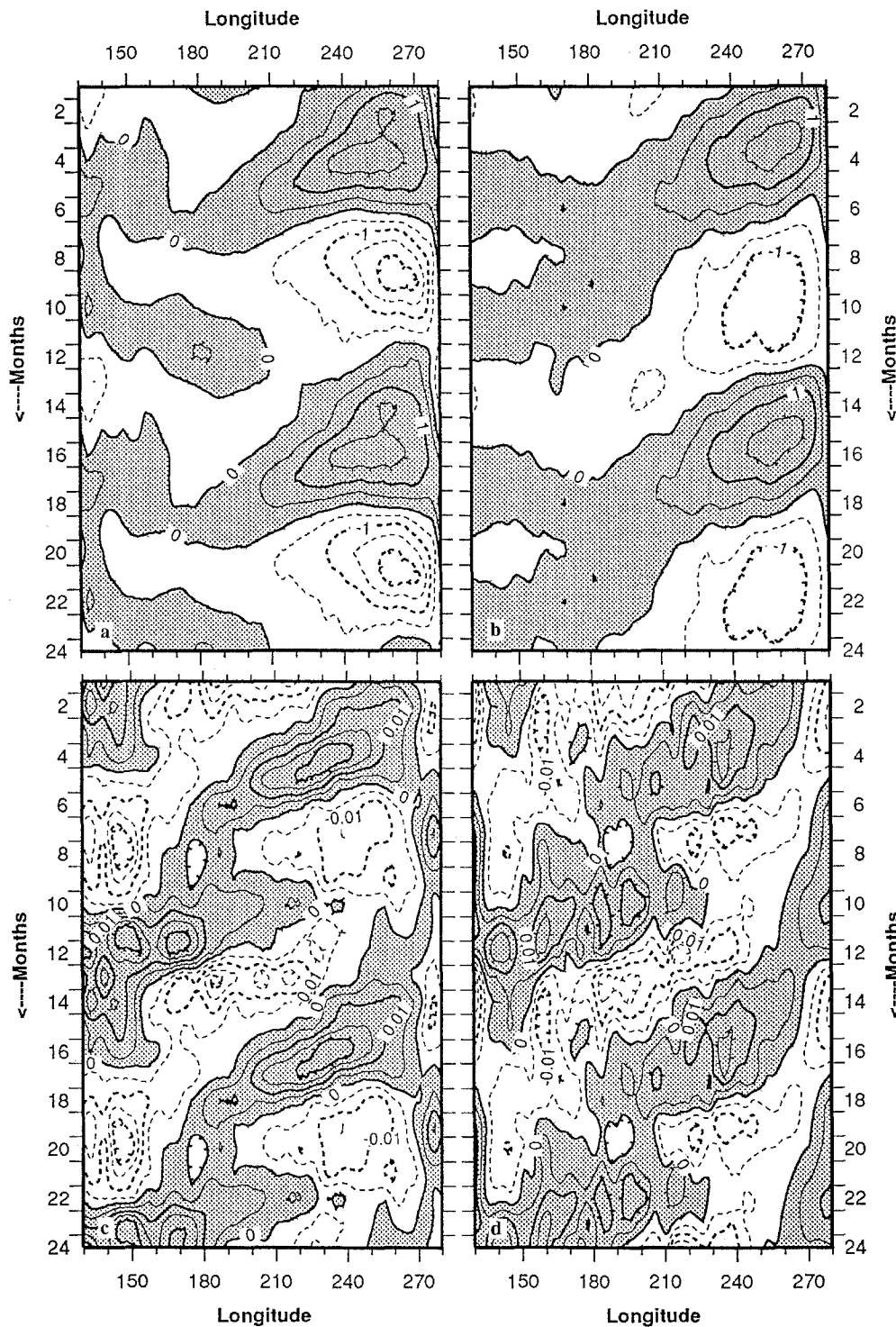


Fig. 9a–d. The mean seasonal cycle of equatorial SST ($^{\circ}\text{C}$) anomalies averaged over (2°N – 2°S). **a** OGCM and **b** OBER climatology. Contour interval is 0.5°C , positive values are shaded. The mean seasonal cycle of equatorial zonal wind stress (Pa) anomalies (5°N – 5°S). **c** AGCM and **d** OBER climatology. Contour interval is 0.005 Pa , positive values are shaded

of these arguments as well as to explore other dynamical processes. The simulated equatorial system is much more symmetric than the observed one as is shown by atmospheric and oceanic surface flow patterns as well as the SST distribution. This symmetry, in striking contrast with the marked asymmetry of the observed system, induces a major heat redistribution within the equatorial ocean which could strongly affect the interannual variability of the system. More precisely, transport by westward currents (SEC, NEC) has decreased

in the coupled simulation compared to the forced one (not shown) while the reverse is true for eastward currents (NECC, EUC and SECC). Therefore, it is not inconceivable that it can inhibit the pile-up mechanism (Wyrtki 1985), which is one necessary condition for ENSO to happen, by preventing warm water accumulating in the western Pacific.

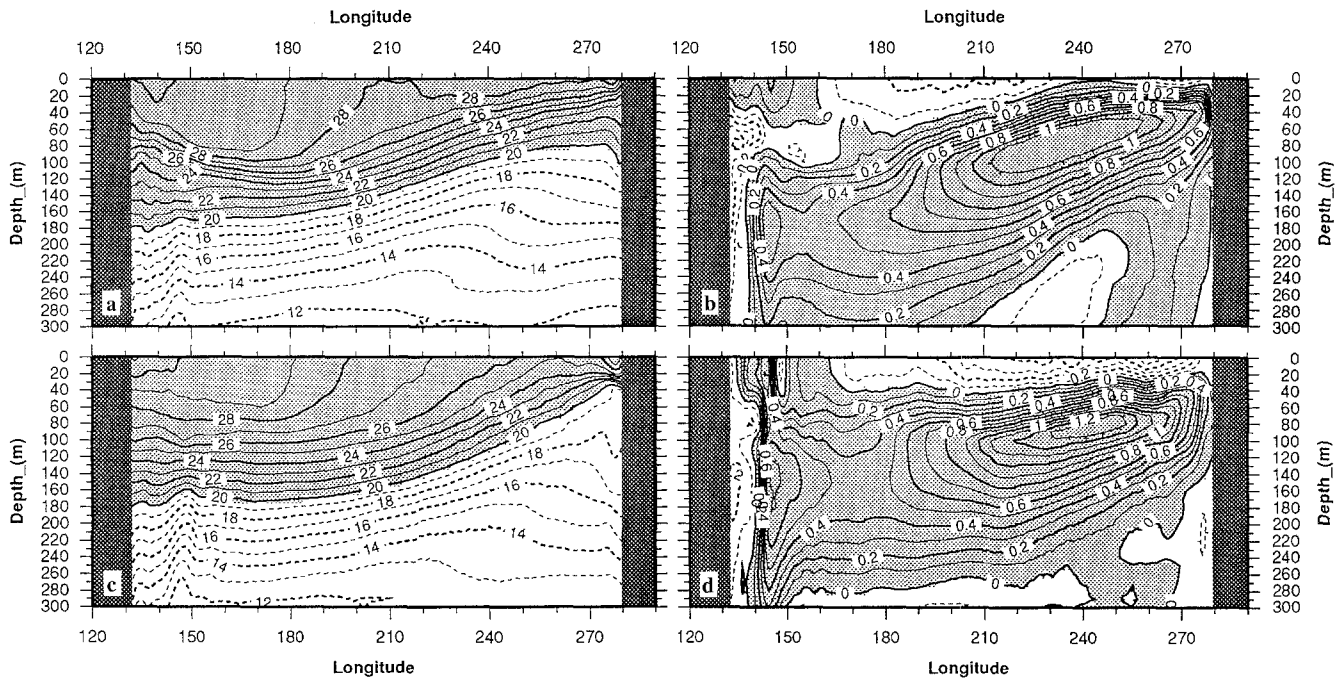


Fig. 10a–d. Equatorial depth-longitude sections of OGCM temperature ($^{\circ}\text{C}$) and zonal current velocity (m s^{-1}) **a, b** April and **c, d** October. Contour interval is 1°C and 10 cm s^{-1} , respectively. *Solid lines* indicate eastward current

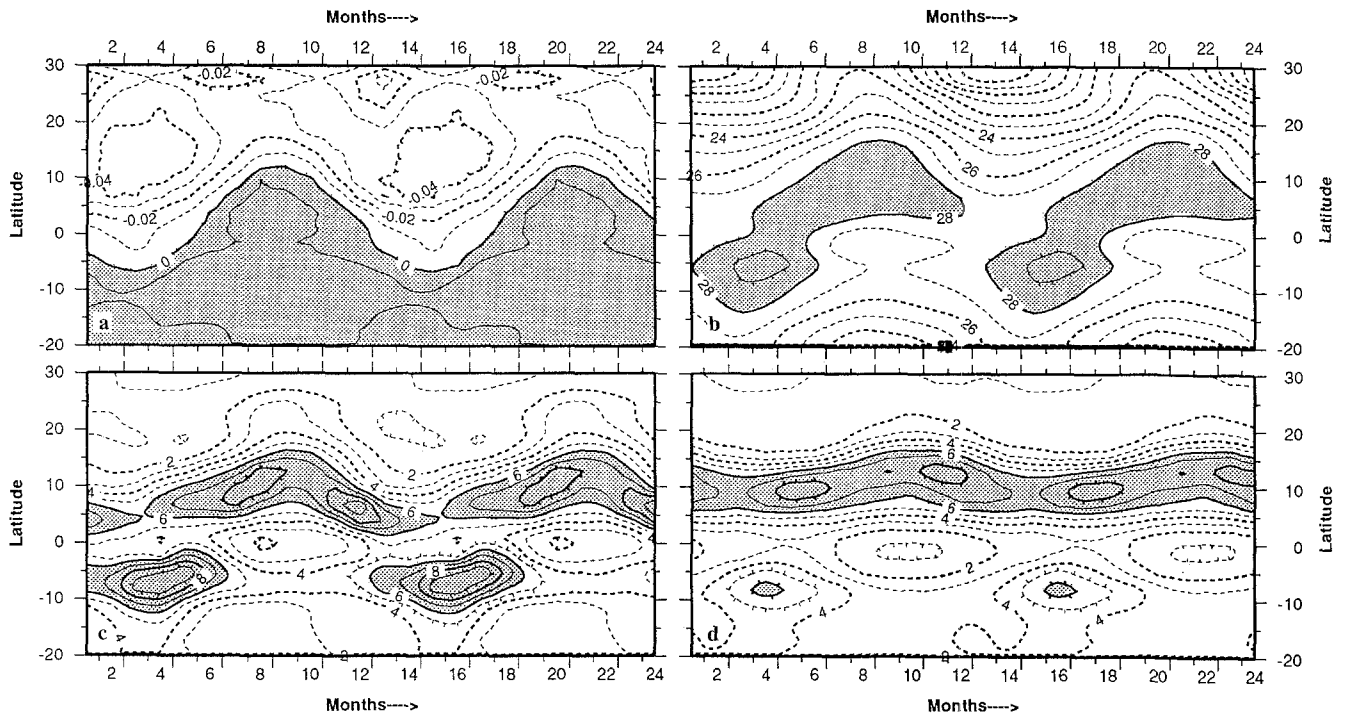


Fig. 11a–d. Time-longitude diagrams (field averaged over 150°W – 100°W ; 20°S – 30°N) of **a** meridional wind stress (AGCM) in Pa. Contour interval is 0.01 Pa and southerly winds are shaded; **b** SST (OGCM) in $^{\circ}\text{C}$. Contour interval is 1°C , shading above

28°C . **c, d** precipitation (AGCM in coupled and uncoupled run) in mm day^{-1} . Contour interval is 1 mm day^{-1} , shading above 6 mm day^{-1}

4 Interannual variability

Figure 12 displays a longitude-time diagram of the equatorial SST and zonal wind stress signals over the 10-year period at the OGCM and AGCM resolution. Although the model is allowed to drift since there is no

flux correction, the simulated climatic state seems rather stable. The most pronounced feature is the seasonal cold tongue in the eastern Pacific. One can hardly discern any trend in the western part of the basin where the SST variation is small (Fig. 12a). The zonal wind stress is westerly over the western Pacific in the north-

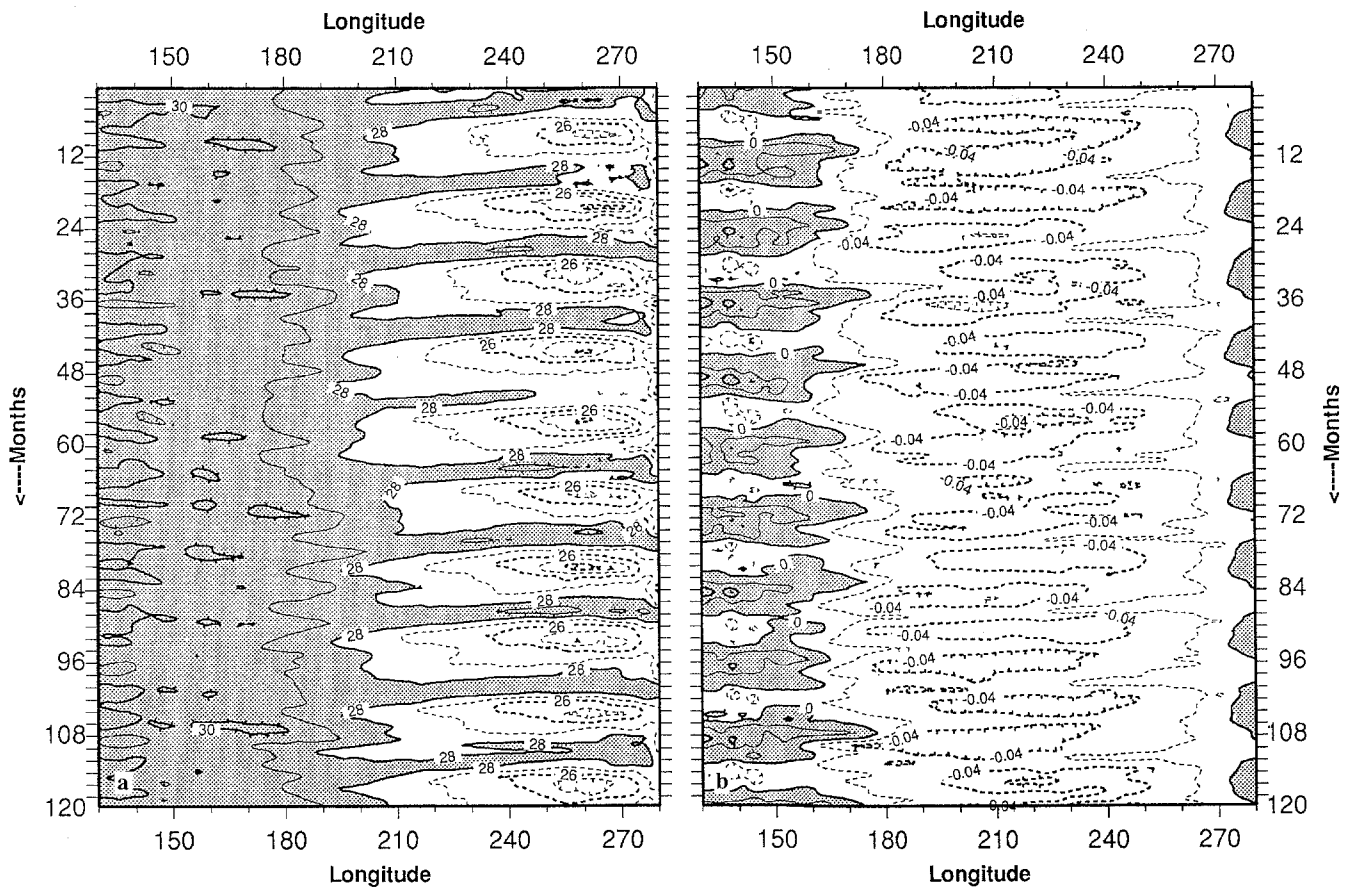


Fig. 12a, b. Variations in **a** SST ($^{\circ}\text{C}$) and **b** zonal wind stress (Pa) along the equator. Contour interval is 1°C and 0.02 Pa , respectively. In shaded regions temperatures exceed 28°C and winds are westerly

ern winter and its interannual variability is rather weak. In the central Pacific, two maxima occur regularly in northern summer and northern winter due to amplification of the southeast and northeast trades, respectively. There is evidence of weak interannual variability. For instance, southeast trades are weaker than usual in the summer of the 6th year. In the eastern Pacific, the pattern is quite regular and exhibits weak spatial gradients. Winds are westerly in the northern summer and diminish towards the far eastern side of the basin (Fig. 12b).

In order to give a better view of low-frequency variability, monthly mean equatorial SST and sea level pressure (SLP) anomalies have been computed and low-pass filtered with the 11-point filter recommended by Trenberth (1984). The filter removes high-frequency components with periods less than eight months and improves the signal-to-noise ratio. In Fig. 13, the simulated (Fig. 13a) and observed (1979–1988) SST anomalies (Fig. 13c) are presented. There is an immediate strong drift to a warmer mean state over a 1-year period. Different mechanisms can be suggested to explain this initial drift. Ocean-atmosphere feedbacks can be responsible for a collapse of the trades since the winds respond to the zonal SST gradient. For instance, an initial warming in the eastern Pacific can weaken the trades which then further reduce the zonal SST gra-

dient and so on. On the other hand, the ocean initial state arises from an uncoupled OGCM simulation with addition of a linear term in SST to the total heat flux forcing. This term can be written as the difference between modelled and observed SST multiplied by a constant (-40 W m^{-2}) and aims at representing to first order the ocean-atmosphere feedbacks in uncoupled simulations. In coupled mode, however, the linear term is no longer added to the net heat flux. The overall result is an additional heat input to the ocean as the coupled model fails to accurately represent the whole set of coupled interactions existing in reality. In particular, the absence of low-level clouds leads to anomalous heating of the upper ocean. The initial warming seen in Fig. 13a illustrates the end of the adjustment process due to the existence of coupled feedbacks and to the heat flux discrepancy. Further analysis is needed to assess the relative importance of these two mechanisms as well as the influence of the initial state.

The CGCM does simulate interannual variability and the irregular oscillation has a time scale of about 3 years as was shown by a multi-channel singular spectrum analysis (M-SSA) by Speich (personal communication). However, the amplitude of the modelled oscillation is 20% that of the typical observed one. Warm SST events, such as the one in years 6–7, initiate in the eastern Pacific and migrate slowly westward with time.

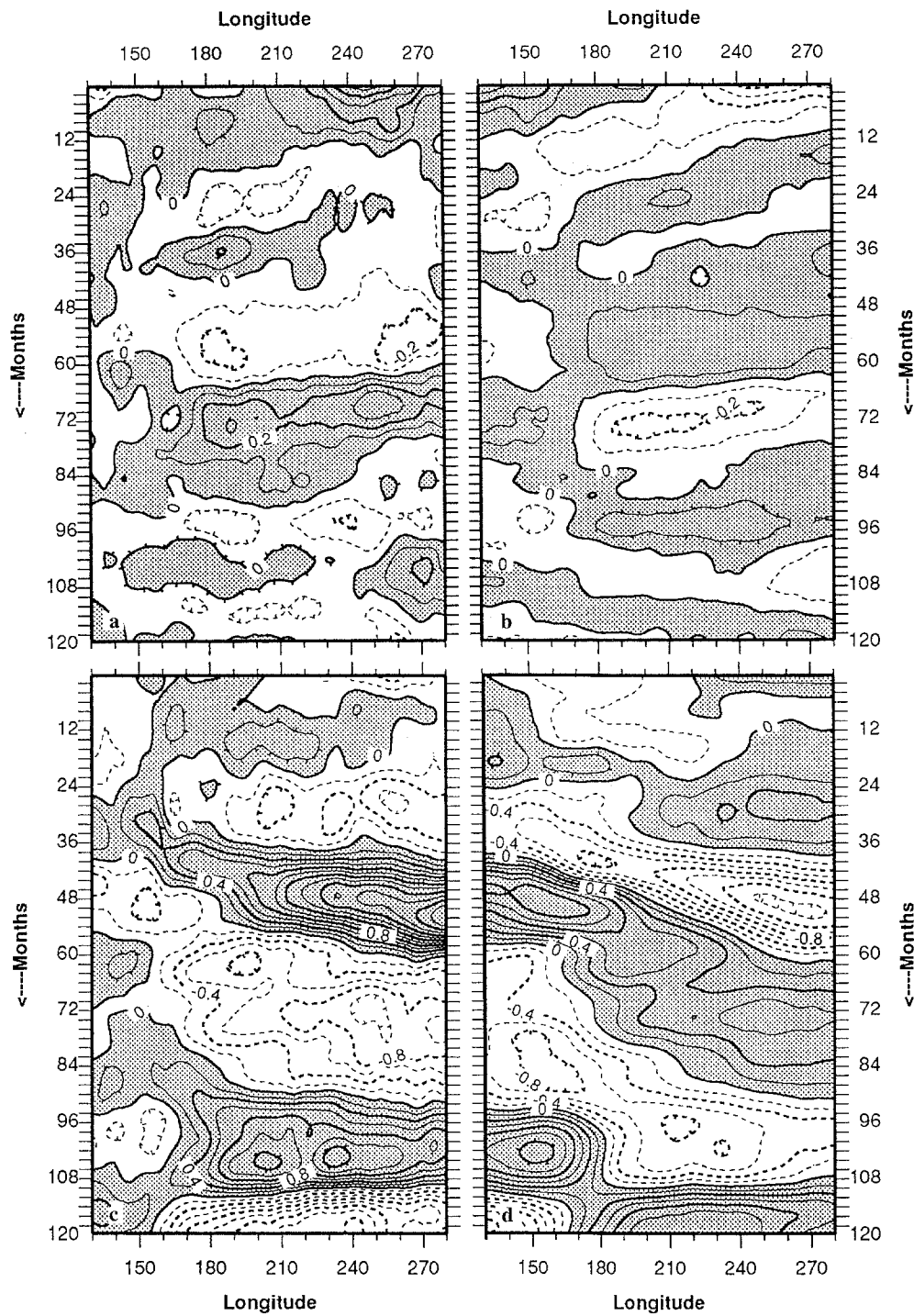


Fig. 13a–d. Time-longitude diagram for the filtered equatorial monthly anomalies averaged in (5°S – 5°N) of simulated: **a** SST ($^{\circ}\text{C}$) and **b** SLP (hPa) with zonal mean removed. Contour interval is 0.1°C and 0.1 hPa , respectively. **c, d** Idem for the observed SST, COLA-CAC data set (1979–1988) and simulated SLP from the AMIP simulation: ARPEGE forced with observed SST over the period (1979–1988). Contour interval is 0.2°C and 0.2 hPa , respectively. Positive values are shaded

The propagation pattern clearly differs from the ones observed during the 1980s where SST anomalies appear first in the central Pacific and then move eastward. Figure 13 displays similarly the SLP anomalies computed from the coupled (Fig. 13b) and the AMIP-type simulations (Fig. 13d). Again, the coupled simulation SLP anomalies are 20% that of the uncoupled ones. The coupled model SLP evolution pattern is coherent with the westward phase propagation of SST and hints at an oscillation mechanism due to air-sea interaction and controlled by advective processes. Figure

13b shows the well-known dipole with opposite changes in the western and eastern hemispheres although the signal amplitude is very weak in the western Pacific. There is anomalous high pressure over the western Pacific and anomalous low pressure over the eastern equatorial Pacific during warm events as in years 6–7 and the opposite for cold ones (years 4–5 and 8–9).

In order to describe more precisely the simulated warm event, the evolution of anomalous oceanic and atmospheric fields is presented and compared to those

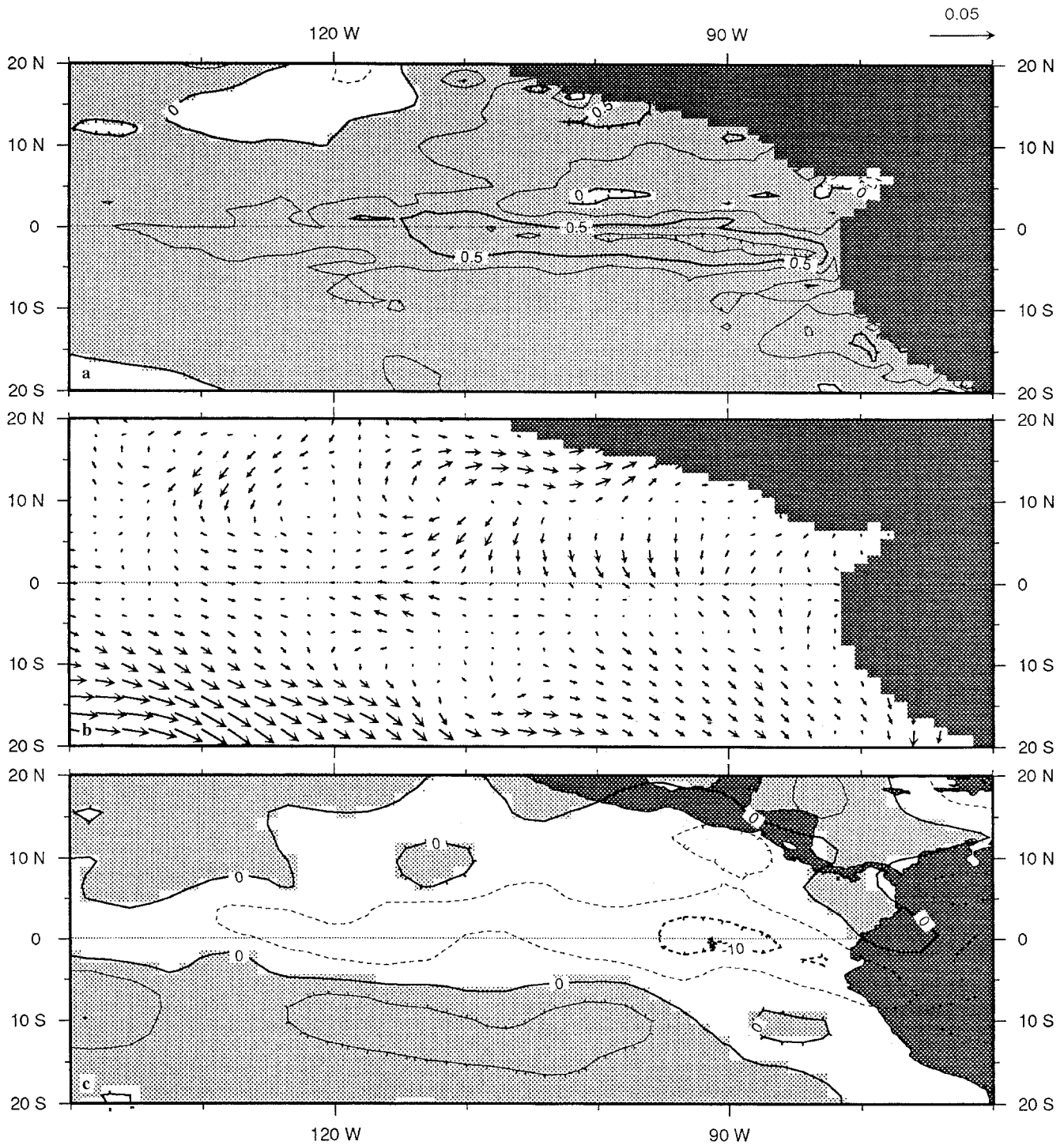


Fig. 14a–c. Simulated June–August anomalies of the 6th year of: **a** SST ($^{\circ}\text{C}$) contour interval is 0.25 $^{\circ}\text{C}$ and *positive* values are *shaded*; **b** surface wind stress (Pa); **c** OLR (W m^{-2}). Contour in-

terval is 5 W m^{-2} and *positive* values are *shaded*. Negative regions indicate enhanced convection

of a composite warm episode as described by Deser and Wallace (1990). Anomalous fields of SST, surface wind stress and outgoing longwave radiation (OLR) will be discussed for the June–August and September–November seasons of the 6th year as well as for December–February and June–August of the 7th year. The March–May season of the 6th year does not exhibit any well defined pattern. In particular, there is no ini-

tial warming along the coast of South America as in the March–May anomaly fields of a typical coastal warm episode (Deser and Wallace 1990).

The most coherent features for the June–August season of the 6th year are situated east of 140 $^{\circ}\text{W}$ and are shown in Fig. 14. The largest positive SST anomalies occur around 2.5 $^{\circ}\text{S}$ and from the coast of South America to 115 $^{\circ}\text{W}$ (Fig. 14a). Northerly wind anomal-

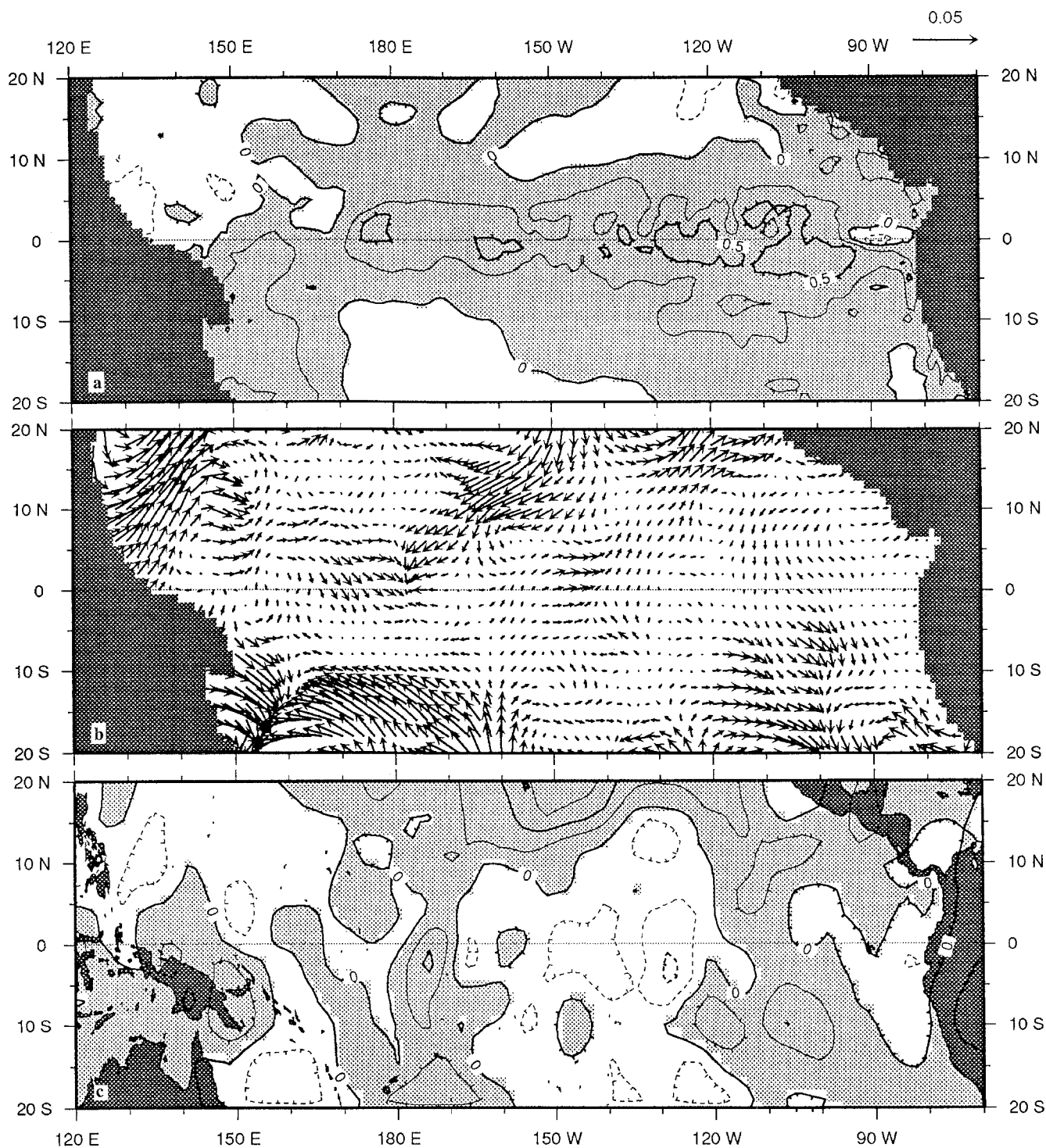


Fig. 15. As in Fig. 14 but for September–November

ies are found between 2°N and 10°N with weaker southerly anomalies just south of the equator (Fig. 14b). These meridional wind anomalies converge over the northern fringe of the equatorial SST anomalies. A band of negative OLR values, indicative of enhanced convection, is centered along 2°N and extends westward to 130°W (Fig. 14c). The strongest wind convergence region corresponds to the area of maximum enhanced convection around 90°W on the equator.

Figure 15 displays the same fields for the September–November season of the 6th year. The core of positive SST anomalies has moved westward and is located between 95°W and 130°W. There is a weaker anomaly maximum in the central Pacific (Fig. 15a). In the eastern Pacific, the wind pattern shows northerly and northwesterly anomalies north and south of the equator, respectively. This indicates light relaxation of the southeast trades. Weak equatorial westerly ano-

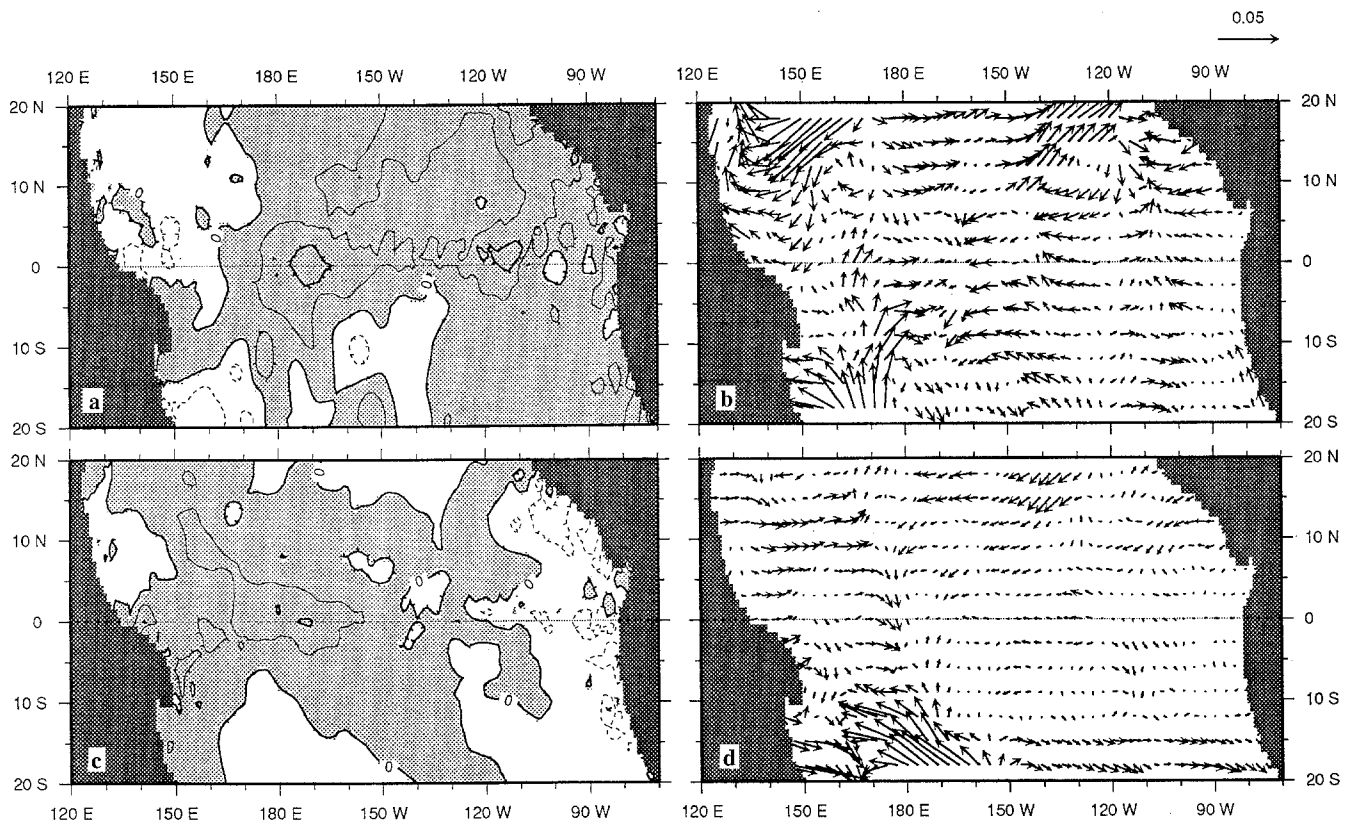


Fig. 16a–d. Simulated anomalies of the 7th year of: **a** December–February SST ($^{\circ}\text{C}$) contour interval is 0.25°C and *positive* values are shaded; **b** December–February surface wind stress (Pa); **c**

June–August SST ($^{\circ}\text{C}$) contour interval is 0.25°C and *positive* values are shaded; **d** June–August surface wind stress (Pa)

malties occur at 140°W converging onto the west end of the marked SST anomalies region. Strong southerly and southeasterly wind anomalies are observed south of the equator in the western Pacific. The southerly anomalies feed the westerly anomalous region in the central Pacific while the southeasterly ones converge onto the southern edge of the SPCZ (Fig. 15b). The OLR anomaly pattern indicates a westward shift of the enhanced convection region which is now located between 120°W and 150°W (Fig. 15c). The simulated SST pattern compares reasonably well with that of the July–November season of the composite warm episode. The simulated anomalous northerly winds are displaced southward compared to the composite. The southerly wind anomalies in the eastern equatorial Pacific found in the composite do not exist in the simulated fields (Deser and Wallace 1990). A possible explanation lies in the displacement and/or the spread of the mean position of the ITCZ south of the equator.

The fields for the December–February season of the 7th year are presented in Fig. 16. The largest positive SST anomalies are centered around 170°W . The SST anomalies have strengthened in the central Pacific and weakened east of 130°W relative to September–November (Fig. 16a). Strong anomalous equatorward flow between 10° and 20° is observed in both hemispheres over the western Pacific. Anomalies are predominantly southeasterly and easterly in the eastern and central eastern Pacific, respectively. This suggests

weak northeast trades. Westerly anomalies converge onto 170°W with the easterlies previously mentioned coinciding with the maximum anomalous SST region (Fig. 16b). The OLR is not included as it does not show any coherent pattern. The simulated patterns of SST and wind fields lack coherency compared to the December–February composite. The simulated SST anomaly maximum is more confined and to the west of the observed composite. The same fields for the June–August season of the 7th year are shown in Fig. 16c, d. Figure 16c illustrates the end of the warm episode in the eastern Pacific with cold anomalies along the coasts of Mexico and South America and extending to 120°W on the equator. A warm residual anomaly centered around 170°W is still present in the central Pacific. The wind pattern exhibits very weak anomalies in the equatorial central and eastern Pacific with weak convergence occurring around 170°W (Fig. 16d). There is a corresponding decrease in OLR over the same region (not shown).

The interannual signal in the coupled model possibly results from air–sea interaction and is also present in the ocean sub-surface. Figure 17 displays the evolution of equatorial dynamic height anomalies over the 10-year period. It shows westward propagation of positive anomalies for the warm event of the 6th year. Despite definite evidence of interannual variability in both the atmosphere and the ocean, its amplitude is clearly smaller than the typical observed values (Busal-

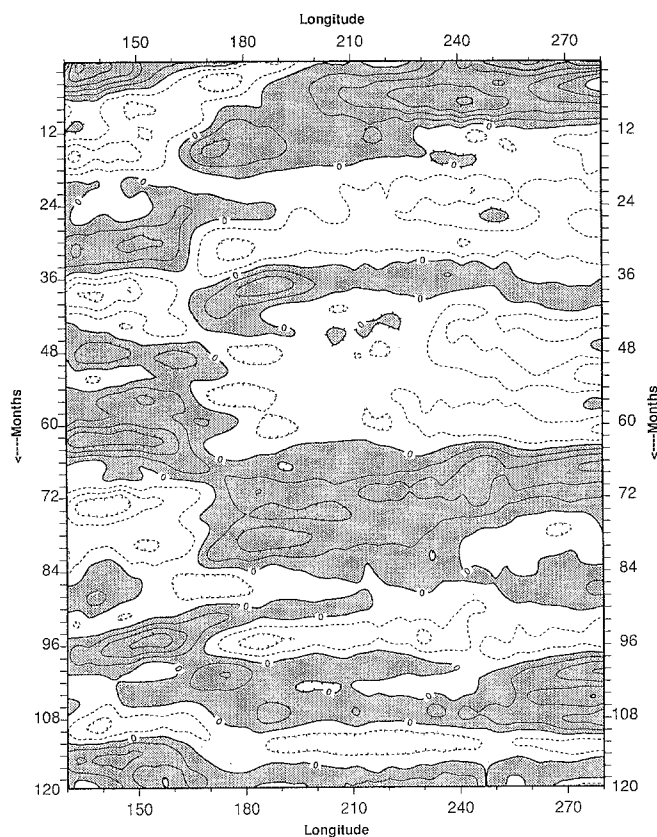


Fig. 17. Time-longitude diagram for the equatorial monthly dynamic height anomalies (cm) averaged in $[5^{\circ}\text{S}–5^{\circ}\text{N}]$. Contour interval is 2 cm and *positive* anomalies are shaded

acchi et al. 1994). Furthermore, the absence of clear signal in the western Pacific both in the atmosphere and ocean sub-surface questions the existence of free oceanic wave mechanisms. Whether the weak signal intensity is related to a warm mean state still awaits definite evidence and further simulations are probably needed to support this claim. As observed ENSO events can be widely different, a longer integration of the coupled model with several warm and cold events is clearly needed to estimate its complete variability spectrum. Furthermore, it must be stressed that the simulation is too short to make definite statements about the relative roles of deterministic and stochastic processes in generating oceanic low-frequency variability.

5 Conclusion

An extended climate integration with a coupled ocean-atmosphere general circulation model (CGCM) has been performed. The CGCM consists of a high resolution tropical Pacific OGCM and a global spectral AGCM at T42 resolution. The model was forced by seasonally varying insolation and the climatology and interannual variability simulated in the tropical Pacific were investigated.

The ARPEGE-OPA coupled model realistically simulates the seasonal cycle over the tropical Pacific ocean despite a warm bias in the ocean mean state. The cold tongue-ITCZ structure is reproduced in the eastern Pacific. In particular, the cold phase of the seasonal cycle is well simulated in phase and amplitude. The warm pool with its seasonal migration is reasonably simulated in the western Pacific. The main features of the equatorial current system are well represented. In particular, the location and intensity of the EUC are in good agreement with the available data. The equatorial thermocline is well defined and the model produces a realistic seasonal variation.

Nevertheless a close inspection of the data reveals some sizable systematic errors generally present in coupled ocean-atmosphere simulations. Atmospheric GCMs with weak trades tend to be associated with oceanic GCMs generating warm SSTs. The ARPEGE-OPA model is no exception to this rule. The mean state of the ocean surface is too warm in the central and eastern Pacific especially along the Californian and Peruvian coasts. The trades are too weak over the entire equatorial Pacific. In the eastern Pacific, the wind stress structure is much too zonal which implies a lack of northward cross-equatorial flow. Reasons for poor behavior in the eastern Pacific can be traced back to deficiencies in both components. Analysis of the coupled run shows an almost complete absence of low level clouds in this region because the boundary layer air is not sufficiently moist. This leads to excessive SST in the eastern regions of the subtropical Pacific ocean due to greatly overestimated solar radiation. The simulated ocean dynamics is also affected by this large amount of heat into the eastern Pacific. Induced changes include intensified eastward currents compared with uncoupled simulations and a marked north-south symmetry of the surface current structure. The belt of warm water flowing eastward south of the equator in northern winter and spring favors the surge of an anomalous convergence zone south of the equator, impacting strongly the wind divergence pattern. The simulated interannual variability is weak compared to observations and exhibits slow westward phase propagation of SST and SLP anomalies.

These aspects are currently being further investigated and sensitivity experiments with the CGCM will be carried on in the near future. In particular, the cloud diagnostic scheme can be tuned to give a sufficient cloud cover over the sub-tropical oceans. Changes in surface fluxes parameterization can be implemented in order to increase the exchange of momentum and humidity at the ocean surface in low wind speed regime. More generally, the atmospheric boundary layer over subtropical oceans requires more study as these areas may be especially significant for coupled atmosphere-ocean climate models. Attention must be given to parameterization of land processes with an interactive ocean instead of fixed SSTs. As the accuracy of surface-flux formulation is clearly essential for climate simulations, emphasis has to be placed also on the marine boundary layer. Specifically, the amount of

water vapor and the cloud distribution in the boundary layer must be simulated accurately. The boundary layer moisture represents the fuel supply for the general circulation while the extent of cloudiness has tremendous effects arising from both latent heating and radiation.

As regards ocean modelling, vertical mixing must be carefully adjusted using the coupled model. Special attention has to be given to its interaction with penetrative solar radiation as these two processes are likely to interplay in the determination of the surface and mixed layer temperatures. The mechanisms responsible for the correct representation of the EUC in the coupled simulation need to be elucidated as they do not seem to agree with the classical argument relying upon large-scale wind forcing. A set of sensitivity experiments could yield considerable insight into the tropical ocean-atmosphere climatology. Finally, if anomalies in the oceanic and atmospheric fields interact non-linearly with the mean state, as seems likely, a better description of the climatology might improve the interannual variability and lead to additional understanding of the ENSO phenomenon.

Acknowledgements. We would especially like to thank David Stephenson for many fruitful suggestions and for carrying out some of the seasonal analysis. We would like to thank Sabrina Speich who completed the M-SSA analysis on the SST data. We are grateful to Alain Braun and Eric Guilyardi for computing support. The GMT graphic software (Wessel and Smith 1991) has been used to produce all the figures. The coupled GCM runs were carried out on the Cray C-90 of Météo-France.

References

- Barnett TP, Graham NE, Cane MA, Zebiak SE, Dolan SC, O'Brien JJ, Legler DM (1988) On the prediction of the El Niño of 1986–1987. *Science* 241:192–196
- Belamari S, Terray L (1993) Simulation of the 1986–1987 El Niño and 1988 La Niña events with a high resolution tropical Pacific ocean general circulation model. CERFACS Techn Rep, CERFACS STR/CMGC/93-30 (to be submitted to *J Phys Oceanogr*)
- Blanke B, Delecluse P (1993) Low frequency variability of the tropical Atlantic ocean simulated by a general circulation model with mixed layer physics. *J Phys Oceanogr* 23:1363–1388
- Bougeault P (1985) A simple parameterization of the large-scale effects of deep cumulus convection. *Mon Weather Rev* 113:2108–2121
- Busalacchi AJ, McPhaden MJ, Picaut J (1994) Variability in equatorial Pacific sea surface topography during the verification phase of the TOPEX/Poseidon mission. *J Geophys Res* 99(C12):24725–24738
- Cane MA, Zebiak SE, Dolan SC (1986) Experimental forecasts of El Niño. *Nature* 321:827–832
- Dandin P (1993) Variabilité basse fréquence simulée dans l'océan Pacifique tropical. Thèse de doctorat de l'université Paris 6
- Delecluse P, Madec G, Imbard M, Levy C (1993) OPA version 7 Ocean General Circulation Model reference manual. LO-DYC, Internal Rep 93/05
- Déqué M, Drevet C, Braun A, Cariolle D (1994) The climate version of Arpege/IFS: a contribution to the French community climate modelling. *Clim Dyn* 10:249–266
- Terray et al.: Climatology and interannual variability simulations
- Deser C, Wallace JM (1990) Large-scale atmospheric circulation features of warm and cold episodes in the tropical Pacific. *J Clim* 3:1254–1281
- ETOP5 (1986) 5' × 5' topography and elevation. Marine Geology and Geophysics Division, National Geophysical Data Center
- Fujio S, Imasato N (1991) Diagnostic calculation for circulation and water mass movement in the deep Pacific. *J Geophys Res* 96:759–774
- Geleyn JF (1987) Use of a modified Richardson number for parameterizing the effect of shallow convection. *J Meteorol Soc Japan*, special NWP Symp Vol:141–149
- Geleyn JF, Hollingsworth A (1979) An economical analytic method for the computation of the interaction between scattering and line absorption of radiation. *Beit Phys Atmos* 52:1–16
- Halpern D, Weisberg R (1989) Upper ocean thermal flow fields at 0°, 28°W (Atlantic) and 0°, 140°W (Pacific) during 1983–1985. *Deep-Sea Res* 36:406–418
- Halpern D, Knox RA, Luther DS, Philander SGH (1989) Estimates of equatorial upwelling between 140°W and 110°W during 1984. *J Geophys Res* 94(C6):8018–8020
- Horel JD (1982) On the annual cycle of the tropical Pacific atmosphere and ocean. *Mon Weather Rev* 110:1863–1878
- Lau NC (1985) Modelling the seasonal dependence of the atmospheric response to observed El Niños in 1962–1976. *Mon Weather Rev* 113:1970–1996
- Levitus S (1982) Climatological atlas of the world ocean, NOAA Prof Pap
- Louis JF, Tiedke M, Geleyn JF (1982) A short history of the operational PBL-parameterization at ECMWF. In: Proc ECMWF Workshop Planetary Boundary Layer Parameterization, 25–27 November 1981, pp 59–80, ECMWF, Shinfield Park, Reading, UK
- Marti O, Madec G, Delecluse P (1992) Comment on “Net diffusivity in ocean general circulation models with non uniform grid”. *J Geophys Res* 97(C8):12763–12766
- McPhaden MJ, McCarthy M (1992) Mean seasonal cycles and interannual variation at 0°, 110°W and 0°, 140°W during 1980–1991. Tech Rep, ERL-PMEL, NOAA 95
- Mechoso CR, Kitoh A, Moorthi S, Arakawa A (1987) Numerical simulations of the atmospheric response to a sea surface temperature anomaly over the equatorial eastern Pacific ocean. *Mon Weather Rev* 115:2938–2956
- Mechoso CR, Robertson AW, Barth N, Davey MK, Delecluse P, Gent PR, Ineson S, Kirtman B, Latif M, Le Treut H, Nagai T, Neelin JD, Philander SGH, Polcher J, Schopf PS, Stockdale T, Suarez MJ, Terray L, Thual O, Tribbia J (1995) The seasonal cycle over the tropical Pacific in general circulation models. *Mon Weather Rev* (in press)
- Miller MJ, Beljaars ACM, Palmer TN (1991) The sensitivity of the ECMWF model to the parameterization of evaporation from the tropical oceans. *J Clim* 5:418–434
- Millero FJ, Poisson A (1981) International one-atmosphere equation of state of sea-water. *Deep-Sea Res* 28A:625–629
- Mitchell TP, Wallace JM (1992) The annual cycle equatorial convection and sea surface temperature. *J Clim* 5:1140–1156
- Neelin JD, Latif M, Allaart MAF, Cane MA, Cubasch U, Gates WL, Gent PR, Ghil M, Gordon C, Lau NC, Mechoso CR, Meehl GA, Oberhuber JM, Philander SGH, Schopf PS, Sperber KR, Sterl A, Tokioka T, Tribbia J, Zebiak SE (1992) Tropical air-sea interaction in general circulation models. *Clim Dyn* 7:73–104
- Oberhuber JM (1988) An atlas based on the COADS data set: the budget of heat, buoyancy and turbulent kinetic energy at the surface of the global ocean. Max-Planck-Institut für Meteorologie Rep 15
- Palmer TN, Mansfield DA (1986) A study of wintertime circulation anomalies during past El Niños events using a high-resolution general circulation model. Part I: influence of model climatology. *Q J R Meteorol Soc* 112:613–638

- Philander SGH, Seigel AD (1985) Simulation of the El Niño of 1982–1983. In: Nihoul JCJ (ed) Coupled ocean-atmosphere models. Amsterdam, Elsevier Oceanography Ser 40:517–541
- Philander SGH, Pacanowski RC, Lau NC, Nath MJ (1991) A simulation of the Southern Oscillation with a global atmospheric GCM coupled to a high-resolution, tropical Pacific ocean GCM. *J Clim* 5:308–329
- Reverdin G, Delecluse P, Levy C, Andrich P, Morliere A, Verstraete JM (1991) The near surface tropical Atlantic in 1982–84. Results from a numerical simulation and a data analysis. *Prog Oceanogr* 27:273–340
- Reynolds RW (1988) A real-time global sea surface temperature analysis. *J Clim* 1:75–86
- Ritter B, Geleyn JF (1992) A comprehensive radiation scheme for numerical weather prediction models with potential applications in climate simulations. *Mon Weather Rev* 120:303–325
- Sarmiento JL, Bryan K (1982) An ocean transport model for the north Atlantic. *J Geophys Res* 87:394–408
- Stephenson D, Royer JF (1994) GCM simulations of the Southern Oscillation for 1979–1988. *Clim Dyn* (in press)
- Terry L (1994) The OASIS Coupler User Guide Version 1.0, CERFACS Technical Report, CERFACS TR/CMGC/94-33
- Trenberth KE (1984) Signal versus noise in the Southern Oscillation. *Mon Weather Rev* 112:326–332
- Unesco (1983) Algorithms for computation of fundamental property of sea water. Unesco Techn Pap Marine Science, 44
- Waliser DE, Gautier C (1993) A satellite-derived climatology of the ITCZ. *J Clim* 6:2162–2174
- Wessel P, Smith WHF (1991) Free software helps map and display data. *EOS Trans Am Geophys Union* 72:441, 445–446
- Wright PB (1988) An atlas based on the COADS data set: field of mean wind, cloudiness and humidity at the surface of the global ocean. Max-Planck-Institut für Meteorologie Rep 14
- Wyrski K (1985) Water displacements in the Pacific and the genesis of El Niño cycles. *J Geophys Res* 90(C4):7129–7132
- Wyrski K, Kilonsky B (1984) Mean water and current structure during the Hawaii-to-Tahiti shuttle experiment. *J Phys Oceanogr* 14:242–254